UNIVERSITY OF AMSTERDAM

UvA-DARE (Digital Academic Repository)

Multi-method Timing of Transient Radio Pulsars with the GBT350 and GBNCC Surveys

Lewis, E.F.; McLaughlin, M.A.; Swiggum, J.K.; Blumer, H.; Boyles, J.; Chawla, P.; Dolch, T.; Hessels, J.W.T.; Kaplan, D.L.; Karako-Argaman, C.; Kaspi, V.; Kondratiev, V.; Levin, L.; Lynch, R.S.; Martinez, J.G.; McEwen, A.E.; Miller, R.; Parent, E.; Ransom, S.M.; Roberts, M.S.E.; Rowe, A.; Spiewak, R.; Stairs, I.H.; Stovall, K.; Thorley, J.; van Leeuwen, J.

DOI
10.3847/1538-4357/ae561d

Publication date
2026

Document Version
Final published version

Published in
Astrophysical Journal

License
CC BY

Link to publication

Citation for published version (APA):
Lewis, E. F., McLaughlin, M. A., Swiggum, J. K., Blumer, H., Boyles, J., Chawla, P., Dolch, T., Hessels, J. W. T., Kaplan, D. L., Karako-Argaman, C., Kaspi, V., Kondratiev, V., Levin, L., Lynch, R. S., Martinez, J. G., McEwen, A. E., Miller, R., Parent, E., Ransom, S. M., ... van Leeuwen, J. (2026). Multi-method Timing of Transient Radio Pulsars with the GBT350 and GBNCC Surveys. *Astrophysical Journal*, *1001*(2), Article 153. https://doi.org/10.3847/1538-4357/ae561d

General rights
It is not permitted to download or to forward/distribute the text or part of it without the consent of the author(s) and/or copyright holder(s), other than for strictly personal, individual use, unless the work is under an open content license (like Creative Commons).

Disclaimer/Complaints regulations
If you believe that digital publication of certain material infringes any of your rights or (privacy) interests, please let the Library know, stating your reasons. In case of a legitimate complaint, the Library will make the material inaccessible and/or remove it from the website. Please Ask the Library: https://uba.uva.nl/en/contact, or a letter to: Library of the University of Amsterdam, Secretariat, P.O. Box 19185, 1000 GD Amsterdam, The Netherlands. You will be contacted as soon as possible.

UvA-DARE is a service provided by the library of the University of Amsterdam (https://dare.uva.nl)

Download date:17 Nov 2026

The Astrophysical Journal, 1001:153 (13pp), 2026 April 20 https://doi.org/10.3847/1538-4357/ae561d
© 2026. The Author(s). Published by the American Astronomical Society.
OPEN ACCESS

Multi-method Timing of Transient Radio Pulsars with the GBT350 and GBNCC Surveys

E. F. Lewis[1,2], M. A. McLaughlin[1,2], J. K. Swiggum[3], H. Blumer[1,2], J. Boyles[4], P. Chawla[5,6], T. Dolch[7,8], J. W. T. Hessels[5,6,9,10], D. L. Kaplan[11], C. Karako-Argaman[10], V. Kaspi[9,10], V. Kondratiev[6], L. Levin[12], R. S. Lynch[13], J. G. Martinez[14], A. E. McEwen[11], R. Miller[1,2], E. Parent[15,16], S. M. Ransom[17], M. S. E. Roberts[8], A. Rowe[1,2], R. Spiewak[12], I. H. Stairs[18], K. Stovall[19], J. Thorley[1,2], and J. van Leeuwen[6]
[1] West Virginia University, Department of Physics and Astronomy, P. O. Box 6315, Morgantown, WV 26506, USA; efl0003@mix.wvu.edu
[2] Center for Gravitational Waves and Cosmology, West Virginia University, Chestnut Ridge Research Building, Morgantown, WV 26506, USA
[3] Department of Physics, Lafayette College, Easton, PA 18042, USA
[4] Department of Physics and Astronomy, Western Kentucky University, 1906 College Heights Blvd., Bowling Green, KY 42101, USA
[5] Anton Pannekoek Institute for Astronomy, University of Amsterdam, Science Park 904, 1098 XH Amsterdam, The Netherlands
[6] ASTRON, Netherlands Institute for Radio Astronomy, Oude Hoogeveensedijk 4, 7991 PD Dwingeloo, The Netherlands
[7] Department of Physics, Hillsdale College, 33 E. College Street, Hillsdale, MI 49242, USA
[8] Eureka Scientific, 2452 Delmer Street, Suite 100, Oakland, CA 94602-3017, USA
[9] Trottier Space Institute, McGill University, 3550 rue University, Montréal, QC H3A 2A7, Canada
[10] Department of Physics, McGill University, 3600 rue University, Montréal, QC H3A 2T8, Canada
[11] Center for Gravitation, Cosmology and Astrophysics, Department of Physics and Astronomy, University of Wisconsin-Milwaukee, P.O. Box 413, Milwaukee, WI 53201, USA
[12] Jodrell Bank Centre for Astrophysics, School of Physics and Astronomy, University of Manchester, Manchester M13 9PL, UK
[13] Green Bank Observatory, P.O. Box 2, Green Bank, WV 24944, USA
[14] Max-Planck-Institut fur Radioastronomie MPIfR, Auf dem Hugel 69, D-53121 Bonn, Germany
[15] Institute of Space Sciences (ICE, CSIC), Campus UAB, Carrer de Can Magrans s/n, 08193, Barcelona, Spain
[16] Institut d'Estudis Espacials de Catalunya (IEEC), Carrer Gran Capità 2–4, 08034 Barcelona, Spain
[17] National Radio Astronomy Observatory, 520 Edgemont Road, Charlottesville, VA 22903, USA
[18] Department of Physics and Astronomy, University of British Columbia, 6224 Agricultural Road, Vancouver, BC V6T 1Z1, Canada
[19] National Radio Astronomy Observatory, 1003 Lopezville Rd., Socorro, NM 87801, USA
Received 2025 December 12; revised 2026 March 10; accepted 2026 March 19; published 2026 April 14

Abstract

We present the timing solutions for three radio pulsars discovered with the Green Bank North Celestial Cap and 350 MHz Green Bank Telescope drift-scan surveys. These pulsars were initially discovered through their single-pulse emissions and are therefore designated as rotating radio transients (RRATs). Follow-up timing campaigns yielded a number of higher signal-to-noise summed pulse profiles for each pulsar, allowing us to obtain timing solutions both through single pulses as well as the standard method of time-integrating the pulsar's emission. We find that the two methods return timing parameters that are usually in agreement within two standard deviations and have similar-sized error bars. The single-pulse timing solutions have significantly higher rms errors and reduced chi-squared values, likely due to pulse jitter. The distribution of wait times between detected single pulses indicates a significant amount of pulse clustering in time on short timescales from all three sources. For all sources, the presence of low-level emissions outside of the sparse bright pulses and the lack of giant pulses is more reminiscent of highly nulling canonical radio pulsars than extremely transient RRATs, highlighting the diversity of emission behavior observed from sources published as RRATs.

Unified Astronomy Thesaurus concepts: Pulsar timing method (1305); Radio pulsars (1353)

1. Introduction

Radio pulsars are rapidly rotating, highly magnetized neutron stars with beams of radio emission extending from their magnetic poles. To date, over 4000 pulsars have been discovered (see, e.g., the ATNF pulsar catalog;[20] R. N. Manchester et al. 2005). Radio pulsars are most often discovered using Fourier-domain periodicity searches, and occasionally in the time domain using fast folding algorithms (e.g., A. D. Cameron et al. 2017; E. Parent et al. 2018).

Rotating radio transients (RRATs), sources emitting isolated radio pulses separated by intervals of minutes to hours, were discovered in single-pulse searches of survey data by M. A. McLaughlin et al. (2006). The pulses from these RRATs obey an underlying periodicity and, like standard radio pulsars, are indicative of radio emission powered by the rotational energy loss of a magnetized neutron star. RRATs are most commonly defined in the literature as pulsars discovered solely through their isolated pulses, as opposed to periodic emission (M. A. McLaughlin et al. 2006; E. F. Keane & M. A. McLaughlin 2011). If RRATs represent a distinct and separate population of neutron stars, their sporadic nature implies the potential for an enormous population of undetected RRATs, to the point that the observed Galactic supernova rate would not be sufficient to produce the expected number of neutron stars (M. A. McLaughlin et al. 2006; E. F. Keane & M. Kramer 2008).

[20] v 2.6.5; https://www.atnf.csiro.au/research/pulsar/psrcat/.

Original content from this work may be used under the terms of the Creative Commons Attribution 4.0 licence. Any further distribution of this work must maintain attribution to the author(s) and the title of the work, journal citation and DOI.

The individual pulses from both pulsars and RRATs display a great deal of temporal variability in their pulse shapes and amplitudes. In addition to stochastic (random) variations of pulsed flux with time, some pulsars display sudden, discontinuous changes in their pulse shapes and fluxes. One manifestation of this phenomenon is nulling, in which the pulsar flux suddenly drops well below the detection threshold, before just as suddenly returning to its usual emission state (N. Wang et al. 2007; S. Burke-Spolaor & M. Bailes 2010). Nulling pulsars display a wide range of intermittency, usually quantified by the nulling fraction, or the fraction of pulses with no detectable emission. It has been suggested that RRATs represent the extreme end of the pulsar intermittency spectrum, or manifest nulling fractions close to 1 (S. Burke-Spolaor & M. Bailes 2010; D. J. Zhou et al. 2023; S.-J. Gao et al. 2025). However, comparisons of the RRAT and nulling pulsar populations have shown that RRATs have longer average spin periods and lower average surface magnetic field strengths; the distributions of these quantities do not appear to be drawn from the same population as those of nulling pulsars, implying that perhaps not all RRATs are just extreme nulling pulsars (Abhishek et al. 2022).

As more sensitive telescopes are built, it will be possible to detect low-luminosity emission outside of the bright pulses from some pulsars originally identified as RRATs, allowing for their detection in periodicity searches. Using the FAST telescope, D. J. Zhou et al. (2023) characterized the emission from newly and previously discovered RRATs, and found that they generally fall into three categories: prototypical RRATs (sporadic, isolated bright pulses separated by long spans with no detected emission), extreme nullers (several successive pulse periods with detected pulses, separated by long time spans of no detectable emission), and standard pulsars emitting low-level emission with sporadic bright pulses. Some RRATs have been observed switching between an RRAT-like and pulsar-like emission state, further indicating how observational sensitivity and the variable emission states of RRATs and pulsars can muddy the attempts to classify these objects based on long-term properties (S. Burke-Spolaor & M. Bailes 2010; S.-N. Sun et al. 2021).

The single-pulse properties of RRATs can clarify their emission states and their relationship to canonical pulsars. For instance, the distribution of pulse energies of most normal pulsars and some RRATs is best described by a log-normal distribution (e.g., S. Burke-Spolaor et al. 2012; B.-Y. Cui et al. 2017; M. B. Mickaliger et al. 2018); conversely, giant pulses with flux densities hundreds to thousands of times higher than the mean flux density have been observed from the Crab Pulsar and a handful of other pulsars, with their energy distribution following a power-law distribution (M. B. Mickaliger et al. 2012; J. van Leeuwen et al. 2020; G. M. Doskoch et al. 2024). Some pulsars and RRATs also show evidence of a power-law tail in their energy distributions, as well as more complex pulse energy distributions (M. B. Mickaliger et al. 2018; D. J. Zhou et al. 2023).

The distribution of wait times between consecutive detected pulses can also be used as a diagnostic to probe the emission processes in pulsars and RRATs. If the wait times between detected pulses were governed by a random process, the probability distribution of the wait times would follow an exponential distribution with a constant pulse rate, which has been observed in RRAT wait time distributions as well as giant pulses from the Crab Pulsar (R. Karuppusamy et al. 2010; B. J. Shapiro-Albert et al. 2018). Some RRATs show evidence of pulse clustering on short timescales, with their wait time distributions exhibiting non-Poissonian behavior (B. J. Shapiro-Albert et al. 2018; M. C. Bezuidenhout et al. 2022; S.-J. Gao et al. 2025). N. Oppermann et al. (2018) showed that a Weibull distribution with a clustering parameter k better fits the pulse arrival times of extragalactic fast radio bursts; $k < 1$ means pulses are more likely to be closely spaced than in the simple Poissonian case.

The rotational period and period derivative, sky coordinates, and other astrometric parameters of a pulsar or RRAT are constrained through the process of pulsar timing (for a more in-depth review, see D. R. Lorimer & M. Kramer 2012). The arrival times of pulses are measured and iteratively fit to a rotational model of the pulsar through least-squares minimization of the residuals, or differences between the observed and predicted arrival times. Pulsar timing accounts for every rotation of the pulsar over the span of the solution, allowing for the measurement of the neutron star's rotational and astrometric parameters with extreme precision. These parameters can then be used to estimate canonical properties of the neutron star such as the surface magnetic field strength and spin-down luminosity. Deriving RRAT timing solutions is therefore crucial for estimating their age and magnetic field strength and characterizing their evolutionary history.

Most pulsars are weak radio emitters, and their individual pulses are not sufficiently brighter than the background noise of the receiver system to allow timing of single pulses. Instead, hundreds to thousands of pulses are added *modulo* the pulse period to form an integrated pulse profile. This has the additional benefit of being more stable in time due to the reduction of intrinsic pulse-to-pulse jitter, or random variations in pulse phase and amplitude (M. T. Lam et al. 2019). In the case of the most sporadic RRATs, however, there are typically not enough detected pulses to add up to create a sufficiently high signal-to-noise summed profile, and timing must be performed through measurements of the single-pulse arrival times (M. A. McLaughlin et al. 2009).

The three pulsars studied in this paper were discovered through their single-pulse emission in survey observations from the 350 MHz Green Bank Telescope (GBT) drift-scan survey (GBT350; J. Boyles et al. 2013; R. S. Lynch et al. 2013) and the Green Bank North Celestial Cap (GBNCC) survey (K. Stovall et al. 2014; A. M. Kawash et al. 2018; R. S. Lynch et al. 2018; R. J. Aloisi et al. 2019; A. E. McEwen et al. 2020). The GBT350 drift-scan survey took place in 2007 when the GBT was undergoing track repairs, and collected over 1491 hr of observations, leading to the discovery of 35 pulsars.[21] The GBNCC scanned the entire Northern sky visible to the GBT, and has discovered[22] 195 pulsars including 24 RRATs. GBT350 and GBNCC discoveries are highlighted in the $P - \dot{P}$ diagram in Figure 1, alongside the three sources studied in this work.

In this paper, we present the timing solutions of three pulsars which were initially discovered only through their RRAT-like single pulses, but which were detectable through

[21] https://astro.phys.wvu.edu/GBTdrift350/
[22] https://astro.phys.wvu.edu/GBNCC/

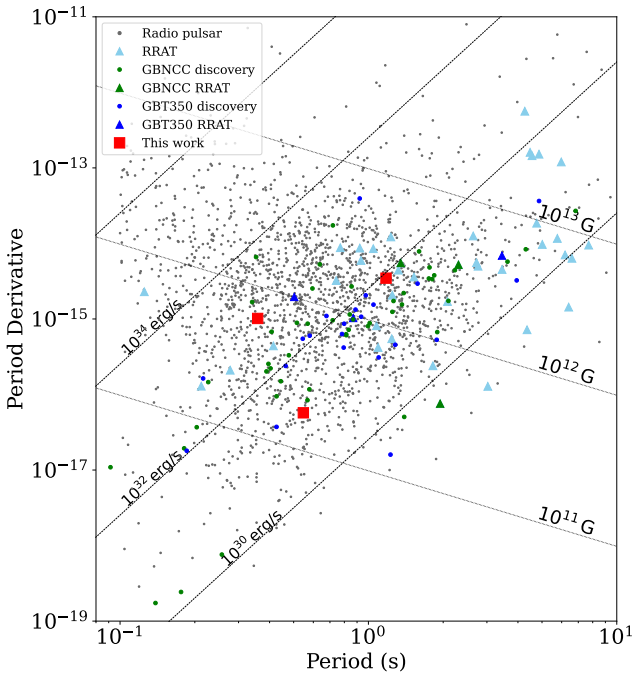

Figure 1. $P - \dot{P}$ diagram showing the population of radio pulsars as a function of rotational period and period derivative. The three sources studied in this work are denoted with red squares. Pulsars and RRATs discovered by the GBNCC survey are labeled in green and those discovered by the GBT350 survey in blue. Lines of constant spin-down energy and constant surface magnetic field are labeled.

periodicity searches at a later date. We compare the efficacy of timing through both integrated profiles and single pulses, and use the single-pulse statistics to draw conclusions about the emission mechanisms at play. We describe the observations in Section 2 and both forms of time of arrival (TOA) generation and timing analysis in Section 3. In Section 4 we describe the single-pulse analysis including the wait time and pulse energy distributions. We discuss our findings in Section 5 and conclude in Section 6.

2. Observations and Data Reduction

The pulsars (PSRs) J0447–0432 (hereafter J0447) and J0539 +0010 (hereafter J0539) were discovered in GBT350 data, although J0539 was never published. The sky position and dispersion measure (DM) of J0447 were reported in C. Karako-Argaman et al. (2015), as well as an estimated rotational period determined through the arrival time differences between detected single pulses. J0539 was also detected by the Commensal Radio Astronomy FAST Survey[23] (D. Li et al. 2018) and labeled on their discovery webpage as PSR J0539+0013, although not published. PSR J1126–2739 (hereafter J1126) was discovered[24] by the GBNCC survey, and identified using the `RRATTrap` single-pulse sifting algorithm[25] (C. Karako-Argaman et al. 2015).

Timing follow-up observations[26] were undertaken between 2014 April and 2020 March using the GUPPI backend (R. DuPlain et al. 2008) on the GBT at 350 and 820 MHz; details of the observational setups are available in Table 1.

Using the PRESTO[27] (S. Ransom 2011) software package, we identified and masked impulsive radio frequency interference (RFI) signals in our data using `rfifind`. In addition, for observations at 350 MHz, persistent RFI occurs in the 360–380 MHz range, and the corresponding channels were ignored in all subsequent analyses.

2.1. TOA Generation—Single Pulses

As pulsar signals travel through ionized material in the interstellar medium, the signal incurs a frequency-dependent delay proportional to the amount of free electrons along the observer's line of sight, with the constant of proportionality known as the DM. A single broadband pulse from a pulsar arrives later at lower observing frequencies compared to higher frequencies, and the data must be dedispersed in order to account for this effect and maximize the detectability of the pulsar signal.

We used PRESTO's `prepdata` function to create a time series from the RFI-mitigated data at a DM of 0 pc cm^{-3}, and `prepsubband` to create many dedispersed time series over a range of DMs centered on the known DM of the pulsar. The DM spacing between time series and the downsampling factor used were calculated using PRESTO's `DDplan.py`, and are given in Table 1. We then used `single_pulse_search.py` to search each time series for pulses, recording any candidate single-pulse events with signal-to-noise ratios (S/Ns) greater than 5. We use an expanded list of boxcar widths in order to be sensitive to a variety of pulse widths, and use a maximum boxcar width which corresponds to a pulse width of 100 ms.

We search over a range of DMs to discriminate astrophysical faint pulses from RFI, as the detected S/N of a single pulse from a pulsar will be decreased if the data are dedispersed at an incorrect DM (J. M. Cordes & M. A. McLaughlin 2003). The S/N is expected to be maximized at the DM of the pulsar, and fall off on either side; thus, even if the single-pulse search code repeatedly identifies the same pulse in multiple dedispersed time series, the grouping of single-pulse events will be closely spaced in time, and the pulse can be identified by choosing the event with the highest S/N.

We observe variations in the DM that maximizes the S/N between single pulses, likely due to radiometer noise, as is evident by the distribution of single-pulse DMs in Figure 2. Thus, to avoid discarding real pulses, we accept single pulses with peak S/Ns at DMs within 10% of the fiducial DM, which is either determined by the peak DM of the brightest astrophysical pulse detected or the DM measured through timing with integrated pulse profiles. In order to mitigate RFI, which may be falsely flagged as a real pulse, a candidate is removed if there is a pulse at a DM of 0 pc cm^{-3} with a greater S/N within one pulse period of the candidate.

Following the timing procedure in M. A. McLaughlin et al. (2009), we created 256 bin pulse profiles for each detected single pulse, and calculated the TOA as the peak of the single-pulse profile. The errors on the TOA are approximated as the width of a bin divided by the S/N of the pulse. We visually inspected each pulse to confirm their astrophysical nature, removing pulses with baselines greatly affected by RFI.

[23] http://crafts.bao.ac.cn/
[24] http://astro.phys.wvu.edu/GBNCC/J1126-27_sp.png
[25] https://github.com/ckarako/rrattrap
[26] Observing programs: AGBT14A_507, AGBT15A_376, AGBT16A_343, AGBT18B_361, AGBT19A_180, AGBT19B_306, and AGBT19B_320
[27] https://github.com/scottransom/presto

Table 1
Observations and Single-Pulse Search Parameters

F_c (MHz)	ΔF (MHz)	t_{samp} (μs)	PSR	N_{obs}	Downsampling Factor	ΔDM (pc cm^{-3})	DM_{low} (pc cm^{-3})	DM_{high} (pc cm^{-3})
350	100	81.92	J0447–0432	8	1	0.01	25	35
			J0539+0010	21	2	0.02	38.5	58.5
			J1126–2739	21	1	0.01	22	32
820	200	40.96	J0447–0432	14	1	0.05	25	35
			J1126–2739	2	1	0.05	22	32

Note. Parameters for the GBT/GUPPI observations of each pulsar at each frequency. From left to right, we list the central observing frequency in MHz, the total observing bandwidth in MHz, the native sampling time, the pulsars observed at that frequency, the number of observations taken of that pulsar at that frequency, the downsampling factor used on the time series, the spacing between different DM trials, and the minimum and maximum DMs searched. No observations of PSR J0539+0010 were taken at 820 MHz.

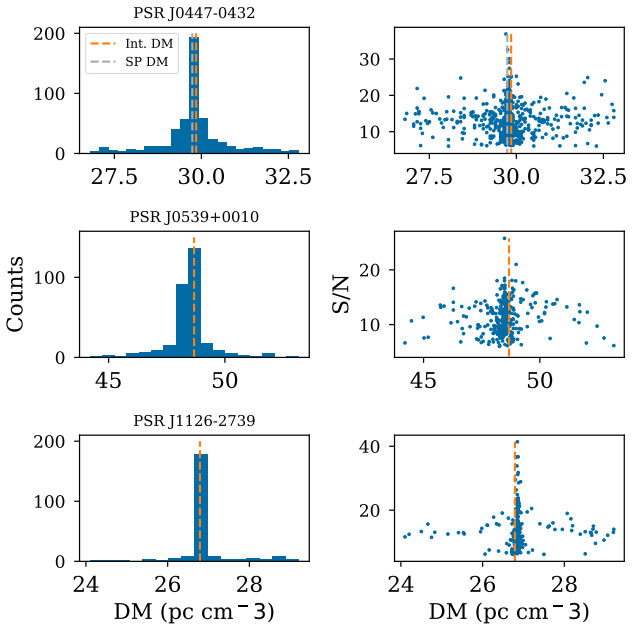

Figure 2. The left column contains a histogram of the best-fit DMs for each single pulse, and the right column shows a scatter plot of the best-fit DM versus the S/N of that pulse reported by PRESTO. For PSR J0447–0432, the orange vertical dashed line represents the DM obtained through timing with integrated TOAs, while the gray dashed line represents the DM obtained through timing with single-pulse TOAs. For the other two pulsars, the pulsar DM was not constrained through timing, and the fiducial DM is shown with an orange vertical dashed line.

2.2. TOA Generation—Integrated Emission

These pulsars were all discovered through their single pulses, but in later follow-up observations, were sufficiently luminous to be detected by an FFT search at several observational epochs. In C. Karako-Argaman et al. (2015), the rotational period of J1126 was constrained using the time differences between detected single pulses, and the quoted rotational period of J0447 was a factor of four longer than the period we report here.

We used the FFT detections as the nominal rotational periods for each pulsar. After folding each observation with 128 phase bins, we combined the profiles for each detection into a high-S/N composite profile; the profiles for each pulsar are shown in the left panel of Figure 3. We then generated TOAs for each observation in which each pulsar was detected using the composite integrated profile as a template and PRESTO's `get_TOAs.py`; the TOA uncertainties were also reported by PRESTO. We generally used only one TOA for each observation except for a "phase-connection" observation, an observation with a high-S/N detection which is closely spaced in time to other observations. An exemplary time-phase plot, integrated pulse profile, and set of single-pulse profiles are presented in Figure 4.

3. Timing Solutions

We used the TEMPO2 software package to obtain all of the timing solutions, using the DE438 solar system ephemeris. We multiplied the uncertainty on each TOA so that the reduced χ^2 value of the postfit timing solution would be equal to 1.

Since we were able to obtain TOAs at both 350 and 820 MHz for J0447, we also fit for DM in the process of pulsar timing, and the reported DM and error are obtained from the timing solution. For J0539 and J1126, we were only able to obtain TOAs at 350 MHz, and thus could not refine the DM measurements through timing. We attempted to fit for the DM by splitting the observing band into subbands and measuring a TOA within each subband; however, performing this analysis on the highest S/N observations for each pulsar did not yield more precise DM measurements than those previously constrained. Instead, we used the `pdmp` function from PSRCHIVE (W. van Straten et al. 2011) to find the optimal DMs for the brightest single pulse for J0539 and J1126, and report those DMs and errors in the sections below.

3.1. PSR J0447–0432

The full timing solution for J0447 is given in Table 2, and the timing residuals are plotted in Figure 5. The derived sky positions and rotational parameters of the two methods are in agreement within two standard deviations.

The rotational period of J0447 was estimated through the single-pulse arrival times in C. Karako-Argaman et al. (2015). According to the reported pulse rate estimates, no more than three pulses would have been detected in a given observation. The use of the greatest common divisor between pulse times as an estimate for an RRAT's rotational period can often lead to a period estimate greater than the true rotational period, and simulations by B.-Y. Cui et al. (2017) show that the probability of determining an incorrect period from three pulses in an observation is roughly 37%; thus, the overestimated period for J0447 is not surprising.

There are five epochs with single-pulse TOAs but no integrated TOA in the timing solutions, and one epoch with an integrated TOA but no single-pulse TOAs. Three of the epochs with only single-pulse TOAs were significantly corrupted by RFI so that an integrated TOA was not obtainable, and the

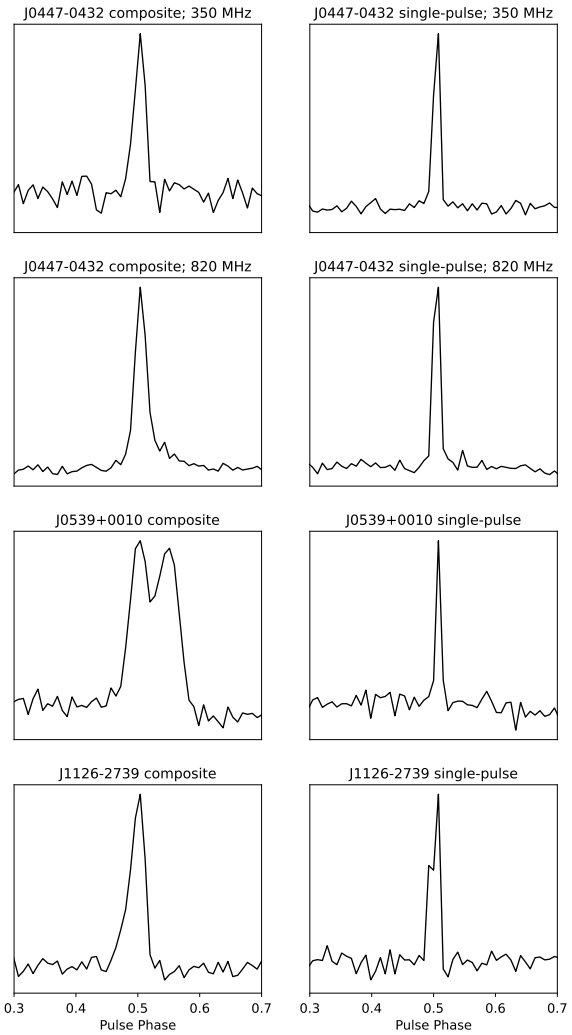

Figure 3. Left: integrated pulse profiles for each pulsar. Right: brightest single pulse for each pulsar. Each profile covers 40% of a single pulsar rotation. The vertical axes are in units of arbitrary intensity.

other two observations were shorter than ten minutes long and yielded a signal that was too weak to reliably measure an integrated TOA. The observation with an integrated TOA but no single-pulse TOAs was at 350 MHz and there were no single pulses with $S/N > 5$ detected by PRESTO; the lack of bright single pulses at 350 MHz is discussed further in Section 4.1.

3.2. PSR J0539+0010

The full timing solution for J0539 is given in Table 3, and the timing residuals are plotted in Figure 6. The derived rotational parameters of the two methods are in agreement within two standard deviations.

The integrated profile of J0539 consistently shows a double-peaked shape across observational epochs. The residuals of the single-pulse TOAs cluster within two main bands, with approximately 17% of pulse residuals falling between the two peaks, and the remainder distributed equally across both bands. The left panel of Figure 7 shows the distribution of the residuals of the single-pulse TOAs, using the best-fit timing solution derived from these TOAs. The bands are centered roughly at pulse phases of ± 0.025, equivalent to ± 29.4 ms from the center of the profile.

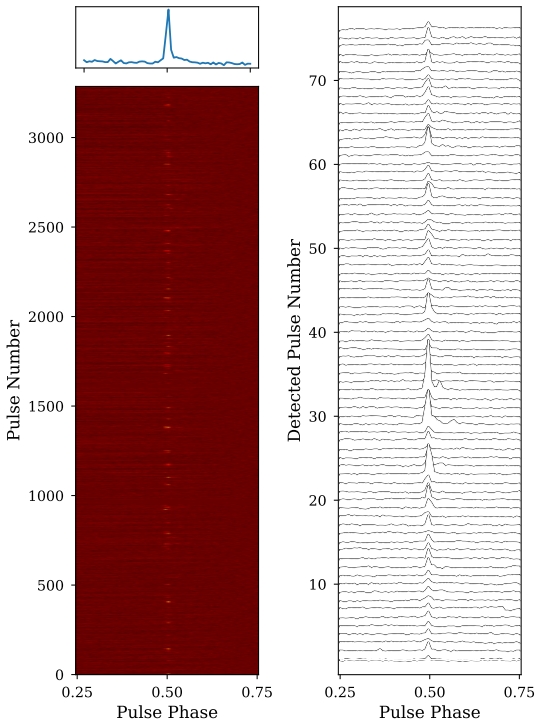

Figure 4. Emission plots for one observation of PSR J0447–0432. Left: a time-phase plot of all 3286 rotation periods in the observation, with the integrated pulse profile above. Right: a sequential pulse stack of the profiles of 75 single pulses from this observation with measured times of arrival in the timing solution.

Pulsar timing methodology is based on the assumption that the pulse originates from the same rotational phase every time. In order to obtain a single-pulse timing solution with lower uncertainties, we first wanted to find the optimal amount by which to shift the TOAs in each band to align the TOAs to a single peak, as in A. G. Lyne et al. (2009). We defined the early and late bands as being composed of TOAs with residuals with absolute values >0.015 in phase, and searched 30 offsets between pulse phases of 0.02 and 0.03 for each band, creating a set of TOAs with the early- and late-band TOAs shifted by the corresponding amount. We chose the offsets corresponding to the set of TOAs which, when run through TEMPO2, yielded the timing solution with the lowest rms residual. This resulted in offsets of 34.9 ms for the early band and 32.5 ms for the late band. The rms residual on the solution decreased from 27.2 ms to 7.2 ms after the TOAs were adjusted, and the uncertainties on the parameters decreased by similar factors.

There are three RFI-impacted epochs with single-pulse TOAs but no integrated TOA in the timing solutions, and there is one epoch with an integrated TOA but no single-pulse TOAs, as no single pulses with $S/N > 7$ were detected by PRESTO, and the few single pulses with $5 < S/N < 7$ were not suitably bright for a reliable TOA measurement.

3.3. PSR J1126–2739

The full timing solution for J1126 is given in Table 4, and the timing residuals are plotted in Figure 8. The rotational parameters of the two methods are in agreement within two standard deviations, and the sky positions are in agreement within 2.5 standard deviations.

There are two RFI-impacted epochs with single-pulse TOAs but no integrated TOA in the timing solutions, and two epochs

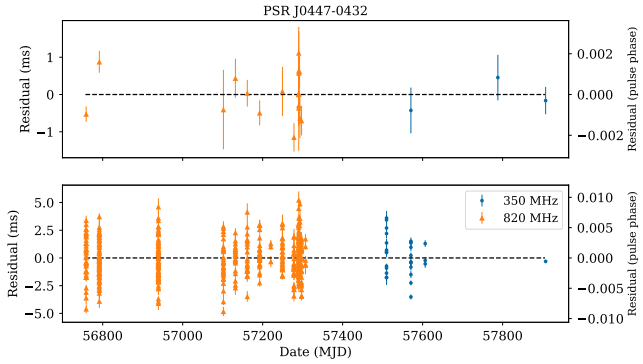

Figure 5. Top: the timing residuals for J0447 using integrated timing. Orange triangles represent the residuals for TOAs at 820 MHz, and blue circles the residuals at 350 MHz. Bottom: the timing residuals for J0447 using single-pulse timing, with the same color mapping.

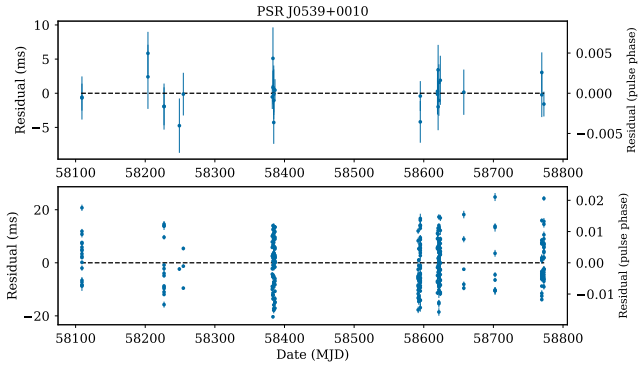

Figure 6. Top: the timing residuals for J0539 using integrated timing. All TOAs have been measured at 350 MHz. Bottom: the timing residuals for J0539 using single-pulse timing. The single-pulse TOAs have been adjusted to a single band, as described in Section 3.2.

Table 2
J0447–0432

	Integrated Timing	Single-Pulse Timing
R.A. (J2000)	$04^h\,47^m\,03\overset{s}{.}89(1)$	$04^h\,47^m\,03\overset{s}{.}881(4)$
Decl. (J2000)	$-04°\,32'\,52\overset{''}{.}9(3)$	$-04°\,32'\,53\overset{''}{.}2(2)$
Spin frequency (Hz)	1.82798530966(7)	1.82798530954(9)
Spin frequency derivative (Hz s^{-1})	$-1.91(1) \times 10^{-16}$	$-1.930(6) \times 10^{-16}$
Dispersion measure (pc cm^{-3})	29.85(5)	29.75(1)
Spin period, P (s)	0.54705034812(2)	0.54705034815(1)
Spin-down rate, $\dot{P}$ (s s^{-1})	$5.72(3) \times 10^{-17}$	$5.78(2) \times 10^{-17}$
Surface magnetic field, B (10^{12} G)	0.18	
Spin-down luminosity, $\dot{E}$ (10^{31} erg s^{-1})	1.4	
Characteristic age, τ_c (Myr)	150	
DM distance (kpc) (NE2001)	1.3	
DM distance (kpc) (YMW16)	0.7	
Data span (yr)	3.14	
Start epoch (MJD)	56758	
End epoch (MJD)	57907	
Timing epoch	57815	
Number of observations	16	21
Number of TOAs	23	512
Postfit residual rms (μs)	596	1549
Reduced chi-squared	2.4	20.2

Note. Timing parameters for the integrated and single-pulse timing models for PSR J0447–0432. 1σ errors are denoted with parenthesis on the last significant digit. The uncertainties have been adjusted with the MODE 1 setting in TEMPO2 so that the final solution has a reduced chi-squared value of 1. Both timing models use the DE438 solar system ephemeris and are referenced to the TT(TAI) time standard.

Table 3
J0539+0010

	Integrated Timing	Single-Pulse Timing
R.A. (J2000)	$05^h\,39^m\,44\overset{s}{.}60(3)$	$05^h\,39^m\,44\overset{s}{.}66(2)$
Decl. (J2000)	$+00°\,10'\,49''\,(2)$	$+00°\,10'\,52''\,(2)$
Spin frequency (Hz)	0.84935705136(5)	0.84935705146(4)
Spin frequency derivative (Hz s^{-1})	$-2.504(5) \times 10^{-15}$	$-2.509(3) \times 10^{-15}$
Dispersion measure (pc cm^{-3})	48.65(2)	
Spin period, P (s)	1.17736115618(7)	1.17736115604(6)
Spin-down rate, $\dot{P}$ (s s^{-1})	$3.470(7) \times 10^{-15}$	$3.478(5) \times 10^{-15}$
Surface magnetic field, B (10^{12} G)	2.0	
Spin-down luminosity, $\dot{E}$ (10^{31} erg s^{-1})	8.4	
Characteristic age, τ_c (Myr)	5.4	
DM distance (kpc) (NE2001)	2.0	
DM distance (kpc) (YMW16)	1.4	
Data span (yr)	1.82	
Start epoch (MJD)	58109	
End epoch (MJD)	58772	
Timing epoch	58384	
Number of observations	17	19
Number of TOAs	29	315
rms postfit residuals (μs)	1950	716
Reduced chi-squared	0.64	61

Note. Timing parameters for the integrated and single-pulse timing models for PSR J0539+0010. 1σ errors are denoted with parenthesis on the last significant digit. The uncertainties have been adjusted with the MODE 1 setting in TEMPO2 so that the final solution has a reduced chi-squared value of 1. Both timing models use the DE438 solar system ephemeris and are referenced to the TT(TAI) time standard.

with an integrated TOA but no single-pulse TOAs, as no single pulses with $S/N > 7$ were detected by PRESTO, and the few single pulses with $5 < S/N < 7$ were not suitably bright for a reliable TOA measurement.

4. Emission Properties

4.1. Pulse Rates

The rate of detected pulses within each observation, defined as the number of single-pulse TOAs divided by the observation length, is shown for all three pulsars in Figure 9. J0447 has consistently higher pulse rates at 820 MHz (mean rate of 132 pulses hr^{-1}) compared to 350 MHz (mean rate of 28 pulses hr^{-1}), which is also clear from the single-pulse residuals in Figure 5. The predicted scattering timescales are roughly 0.4 and 730 μs at 820 and 350 MHz, respectively, so the signal is not scattered out at lower frequencies, and we do not see strong scattering tails in the profiles of this pulsar at 350 MHz (e.g., Figure 3).

To determine whether the difference in pulse rates is due to an intrinsic emission effect or observational sensitivity, we

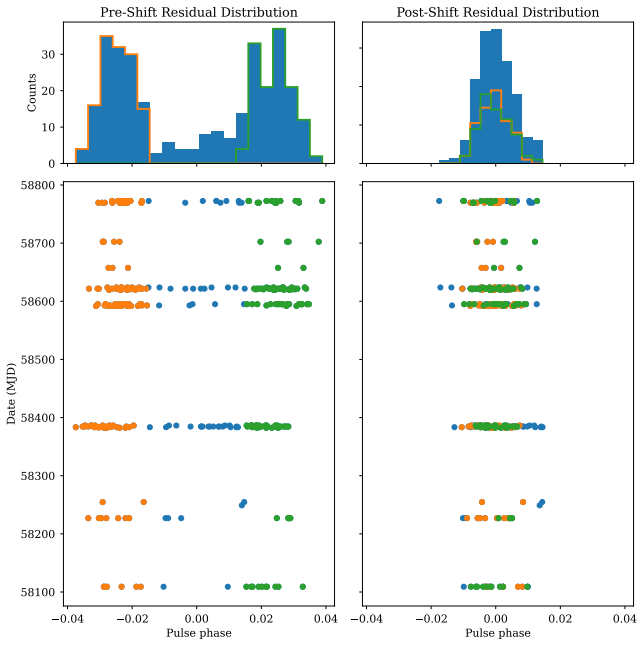

Figure 7. Left: the distribution of timing residuals from the TOAs of the single pulses from PSR J0539+0010 over the 1.8 yr observational campaign, with the residuals as a function of MJD plotted below. The TOAs tend to cluster in two peaks, denoted by orange and green, respectively. Right: the distribution of timing residuals from the same TOAs, after adjusting the TOAs as described in the text. The TOAs originally in the early or late band are still denoted by orange and green, respectively.

calculate the minimum flux ($S_{\rm min}$) necessary to detect a 10 ms duration pulse at an S/N of 6 in each observing band using the radiometer equation:

$$S_{\rm min} = \frac{({\rm S/N_{min}})\,T_{\rm sys}}{G\sqrt{n_P \Delta\nu W_{\rm obs}}}, \quad (1)$$

where we use constant values of ${\rm S/N_{min}} = 6$, a gain of $G = 2$ K Jy^{-1}, and two recorded polarizations ($n_P = 2$).

At 350 MHz, a system temperature[28] of $T_{\rm sys} = 46$ K and a working bandwidth of $\Delta\nu = 80$ MHz imply a single-pulse flux detection threshold of 109 mJy. At 820 MHz, assuming a system temperature of 35 K and a bandwidth of 200 MHz yields a minimum flux of 52 mJy. We also used the radiometer equation to estimate the mean flux of J0447 in each observation from the S/N of the folded profile, replacing $W_{\rm obs}$ with the observation time in seconds. We find an average flux of 56 ± 35 mJy at 820 MHz and 49 ± 21 mJy at 350 MHz, where the error represents the standard deviation of all of the flux estimates at that frequency.

Assuming that J0447 follows a simple spectral power law with the average pulsar spectral index of −1.6 (F. Jankowski et al. 2018), the mean flux at 350 MHz would be roughly 4 times higher than that at 820 MHz, and we would expect roughly twice as many single pulses exceeding the detection threshold at 350 MHz than at 820 MHz, given the higher detection threshold. Conversely, the detected pulse rate at 820 MHz is on average 4.5 times greater than the pulse rate at 350 MHz, though the time-averaged fluxes are very similar between the two frequencies. We thus conclude that there are fewer, though brighter, detected single pulses at 350 MHz compared to at 820 MHz where the single-pulse detection threshold is lower.

[28] https://gbtdocs.readthedocs.io/en/latest/references/receivers.html

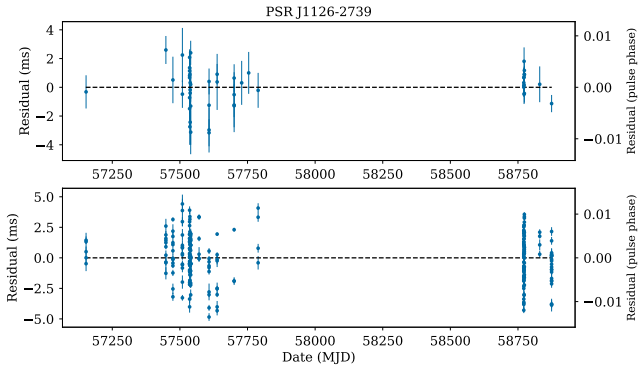

Figure 8. Top: the timing residuals for J1126 using integrated timing. All TOAs have been measured at 350 MHz. Bottom: the timing residuals for J1126 using single-pulse timing.

Table 4
J1126–2739

	Integrated Timing	Single-pulse Timing
R.A. (J2000)	$11^{\rm h}\,26^{\rm m}\,29\overset{\rm s}{.}18(2)$	$11^{\rm h}\,26^{\rm m}\,29\overset{\rm s}{.}25(1)$
Decl. (J2000)	$-27°\,39'\,56\overset{''}{.}3(3)$	$-27°\,39'\,56\overset{''}{.}1(2)$
Spin frequency (Hz)	2.79207295863(4)	2.79207295872(3)
Spin frequency derivative (Hz s^{-1})	$-7.921(2) \times 10^{-15}$	$-7.920(1) \times 10^{-15}$
Dispersion measure (pc cm^{-3})	26.85(6)	
Spin period, P (s)	0.358156830004(4)	0.358156829992(4)
Spin-down rate, $\dot{P}$ (s s^{-1})	$1.0160(2) \times 10^{-15}$	$1.0159(2) \times 10^{-15}$
Surface magnetic field, B (10^{12} G)	0.610	
Spin-down luminosity, $\dot{E}$ (10^{31} erg s^{-1})	87.3	
Characteristic age, τ_c (Myr)	5.6	
DM distance (kpc) (NE2001)	1.1	
DM distance (kpc) (YMW16)	0.4	
Data span (yr)	4.7	
Start epoch (MJD)	57153	
End epoch (MJD)	58874	
Timing epoch	58013	
Number of observations	19	21
Number of TOAs	49	237
rms postfit residuals (μs)	1100	1742
Reduced chi-squared	1.91	54.8

Note. Timing parameters for the integrated and single-pulse timing models for PSR J1126–2739. 1σ errors are denoted with parenthesis on the last significant digit. The uncertainties have been adjusted with the MODE 1 setting in TEMPO2 so that the final solution has a reduced chi-squared value of 1. Both timing models use the DE438 solar system ephemeris and are referenced to the TT(TAI) time standard.

4.2. Wait Times and Pulse Clustering

We used the measured arrival times of each pulse to create a wait time distribution, excluding any wait times between observations due to their sporadic cadence. The Poisson distribution has a probability density function of $A^*r_P^*e^{-r_P*t}$ at a wait time t, with an arbitrary amplitude A and Poissonian pulse rate r_P. The Weibull distribution is an extension of the Poissonian case using a clustering parameter k, and has a

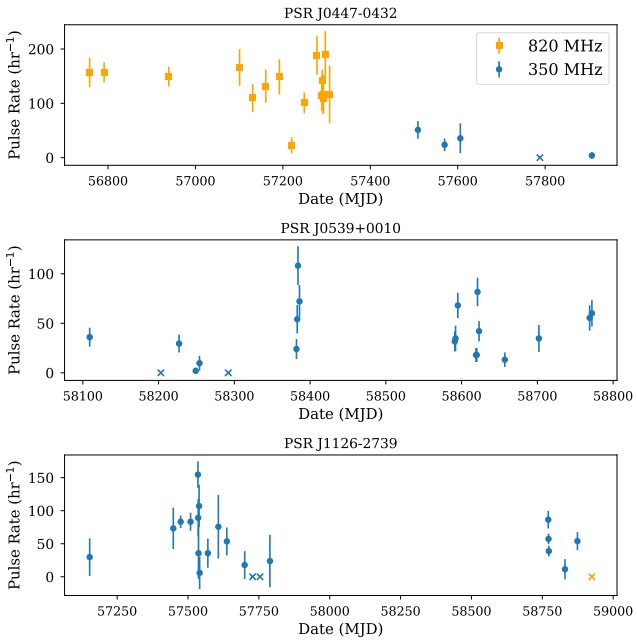

Figure 9. The detected pulse rates for each observation of PSRs J0447–0432 (top), J0539+0010 (middle), and J1126–2739 (bottom). Observations at 820 MHz are marked with orange squares, and observations at 350 MHz with blue circles. Observations with no detected emission are marked with an "x" in the color corresponding to the central frequency of the observation. The error bars correspond to 1σ error bars corresponding to Poissonian statistics (N. Gehrels 1986).

Table 5
Wait Time Distribution Fit Parameters

PSR	r_P (hr^{-1})	r_W (hr^{-1})	k	FP
J0447–0432	220 ± 20	130 ± 40	0.5 ± 0.1	3×10^{-7}
J0539+0010	97 ± 6	56 ± 7	0.49 ± 0.05	9×10^{-15}
J1126–2739	93 ± 10	58 ± 15	0.65 ± 0.09	7×10^{-4}

Note. The wait time distribution fit results: r_P is the Poissonian pulse rate, r_W the Weibull pulse rate, and k the Weibull clustering parameter. The final column denotes the probability that the improvement to the fit from the Weibull distribution is due to random chance. 1σ errors are denoted.

probability density function

$$\frac{Ak}{t}*[t*r_W*\Gamma(1+1/k)]^{k}*e^{-[t*r_W*\Gamma(1+1/k)]^{k}}, \quad (2)$$

where Γ represents the gamma function (N. Oppermann et al. 2018).

We fit Poisson and Weibull distributions to each distribution using `scipy.optimize.curve_fit` and report the results of each fit in Table 5. The number of bins in each distribution were chosen using the Freedman Diaconis estimator. The wait times, in units of pulsar rotations, are shown in Figure 10 along with the fitted statistical distributions.

The distribution of wait times from J0447 shows slight evidence of a secondary peak of wait times centered at around 75 periods, although the inclusion of a Maxwell–Boltzmann or Gaussian component did not yield a statistically significant improvement in the quality of the fit. Similar secondary "bumps" in the wait time distribution were observed in PSRs J1317–5759 and J1819–1458, with increased wait times at ∼25 pulse periods, although no statistical distribution was able to fully describe the bumps in the distribution, likely due to the complex nature of the wait time distributions (B. J. Shapiro--Albert et al. 2018).

Since only the TOAs from the timing analysis were used to calculate the wait times, low-luminosity pulses would not be considered, potentially introducing a bias toward longer wait times. Additionally, excising rotations corrupted by RFI could cause astrophysical pulses to be excised, artificially increasing the reported wait times. To measure the effect of the long-wait tails on the distribution fits, we reran the wait time analysis only on wait times shorter than a given threshold; cutoff thresholds of 200, 250, and 500 rotational periods each yielded results in agreement with those reported in Table 5. Overall, we find that the Weibull distribution with $k < 1$ is preferred for all three pulsars, indicating that pulse clustering on short timescales is present.

We performed a statistical F-test to compare the goodness of fit of the two distributions and determine if adding the extra parameter in fitting the Weibull distribution makes a statistically significant improvement to the fit. The F-test returns a statistic which we use to determine the probability that the improvement to the fit is due to random chance. These false alarm probabilities are presented in the final column of Table 5, and indicate that the wait times from J0539 are much better fit by a Weibull distribution, and the same is true to a lesser extent for J0447. We conclude that significant amounts of pulse clustering are present in the emissions from PSRs J0447 and J0539, and that the pulse clustering model may be preferred for PSR J1126, but with lower certainty.

4.3. Pulse Energy Distributions

We determined on-pulse and off-pulse regions for each pulsar by visible inspection of their time-phase plots. For each pulse, the on-pulse energy and off-pulse standard deviation were calculated and normalized by the average on-pulse energy of all rotations from that observation. The resulting distributions are shown in Figure 11 (left panel). In nulling pulsars of sufficient brightness, such a distribution naturally separates into two distinct components (see, e.g., A. G. J. van Leeuwen et al. 2002), allowing an unambiguous distinction between pulses with and without emission. In these three cases, however, the energy distributions are continuous. We choose $S/N > 2$ as the boundary and study the pulse energy distribution of pulses exceeding that. The pulse energies of all these pulses with $S/N > 2$ are next plotted for each pulsar in the right panel of Figure 11, alongside the best-fit log-normal and power-law distributions fit using `scipy.optimize.curve_fit`. A combined log-normal and power-law distribution was also tested, but led to worse fits for all three pulsars, so we do not plot them.

The fit results indicate that a power-law distribution is preferred over a log-normal energy distribution for all three pulsars in this sample. A power-law tail in the energy distribution implies the presence of giant pulses; however, giant pulses from the Crab Pulsar and others are several orders of magnitude brighter than the average pulsed flux. We do not see such a pronounced increase in pulse energy in the brightest pulses from this sample, with only one pulse from J1126 being greater than 10 times more energetic than the average pulse energy. The lack of exceptionally bright pulses leads us to conclude that the emission mechanisms are more similar to the standard pulsar model, as opposed to giant pulse emission,

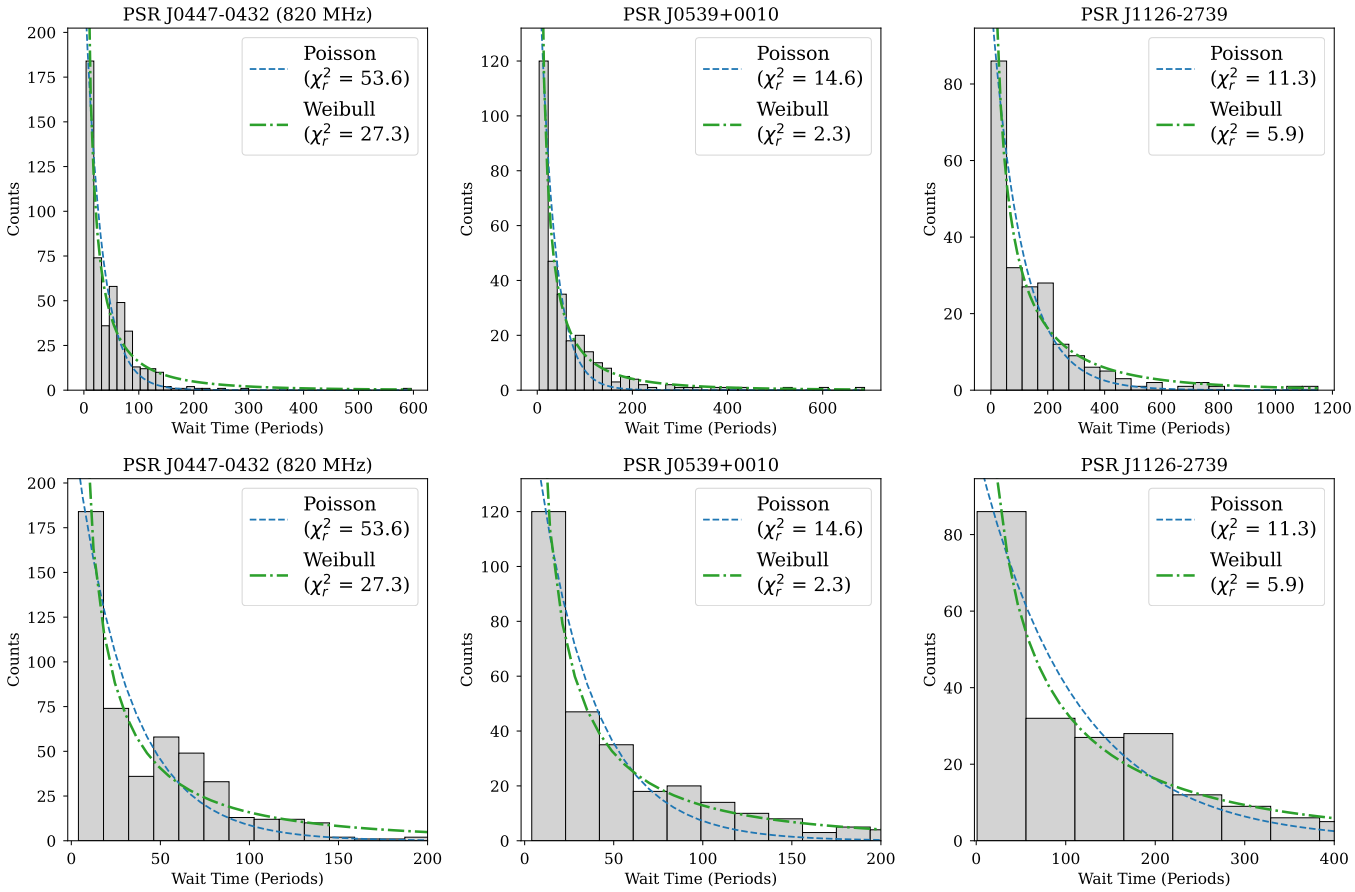

Figure 10. Wait time distributions for all three pulsars studied in this paper. The best-fit Poisson distribution is overlaid with a blue dashed line, and the best-fit Weibull distribution in a dotted–dashed green line. The bottom row displays the same distributions and analytical fits as the top row, zoomed in to show only the first 200 or 400 periods.

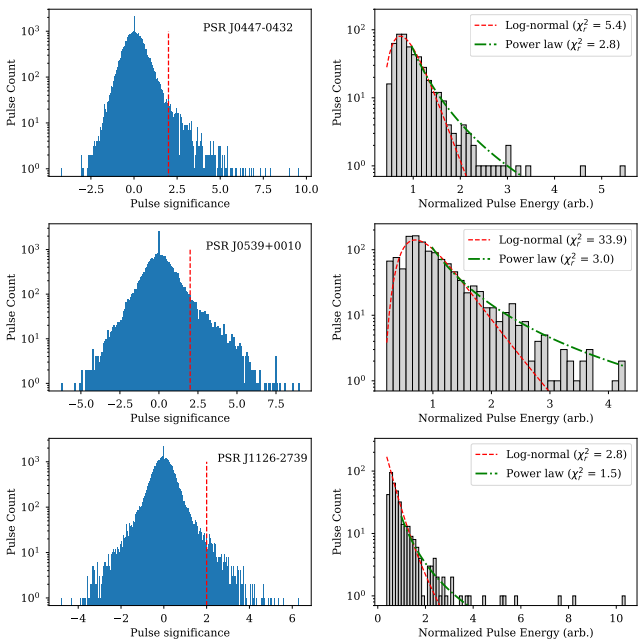

Figure 11. The pulse energy distributions for all three pulsars studied in this paper. Left: the distribution of on-pulse S/N for every rotation observed from each pulsar. The red dashed lines denote cutoffs of S/N = 2. Narrow peaks at S/N = 0 correspond to RFI-corrupted data which have been masked. Right: the distribution of pulse energies for all pulses with S/N $\geqslant$ 2. The best-fit log-normal distribution is overlaid with a red dashed line, and the best-fit power-law distribution in a dotted–dashed green line.

despite the slight preference for power-law distributions. We also examined the pulse energies as a function of the wait time between detected pulses finding no correlation, suggesting that energy is not being stored up between pulses.

4.4. Weak Emission

Characterization of the emission properties of many pulsars by the FAST GPPS survey grouped them into three loose groups: the majority of RRATs are "normal" pulsars with occasional bright pulses, some are extreme nullers, and some show very few bright pulses with no weak emission (D. J. Zhou et al. 2023). To determine the emission patterns of these pulsars, we used the dedispersed data cubes to create time-phase plots and total integrated profiles for each observation. We then extracted all subintegrations with S/Ns > 2, and created profiles exclusively from those pulses, as well as a "noise" profile consisting only of subintegrations with S/N < 2, which are shown in Figure 12. While the majority of the emission comes from the sporadic, bright pulses, each pulsar shows evidence of subthreshold emission, particularly J0447.

5. Discussion

5.1. Timing

We successfully obtained phase-connected timing solutions for these three pulsars using the standard method of integrating the emission by folding the data, as well as by

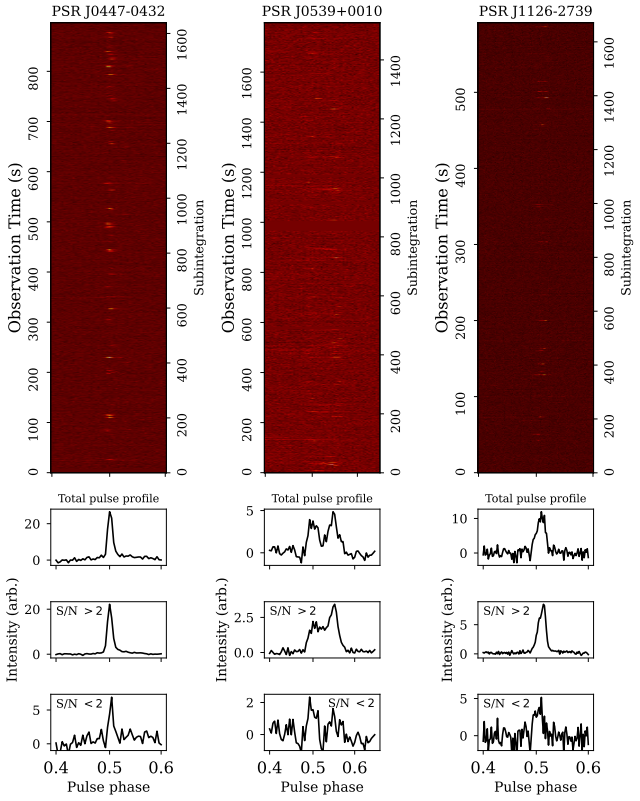

Figure 12. Characteristic observations of each pulsar. The top row displays a time-phase plot from one observation of each pulsar. Below, the total integrated profile, profile composed of only subintegrations with S/N > 2, and profile composed of only subintegrations with S/N < 2. Each plot covers only 10% to 20% of a full rotation.

measuring TOAs for each detected single pulse. The independently obtained sets of TOAs provide an opportunity to cross-reference the derived timing parameters between solutions and evaluate the accuracy and precision of the two timing methods.

For all three pulsars, the single-pulse timing solutions have larger rms postfit residuals and larger reduced chi-squared values,[29] suggesting that these timing models fit the observed TOAs less accurately, and that there would be more uncertainty in the derived parameters making up the timing model. However, the timing-derived parameters have error bars of similar sizes and are generally in good agreement between the two timing methods for all three pulsars. To visualize this, we have plotted the period and period derivative (Figure 13) and the sky positions (Figure 14) returned by the best-fit timing models for each pulsar using both methods, as well as the error bars on each. All of the parameters are in agreement between the two solutions within two standard deviations. This indicates that the timing solutions are of comparable accuracy. The error bars on the parameters from single-pulse timing are consistently less than or equal to the error bars on the same parameters from the integrated timing solution; the greater number of TOAs and detection of single pulses on epochs without folding detections likely allowed for more accurate constraints on these parameters.

[29] Using the MODE 1 setting in TEMPO2, the uncertainties on the TOAs were multiplied by a factor so that the reduced chi-squared values of the final solutions would be 1.

The two methods studied here yield spin parameters and sky positions with similar-sized error bars, yet the rms and reduced chi-squared values (χ^2_r) of the single-pulse solutions are significantly higher due to the large number of TOAs scattered across a larger pulse phase envelope. To perform the fits, TEMPO2 first measures the residual of each pulse and the difference between the predicted and observed arrival times based on the provided prefit timing model. TEMPO2 uses a weighted least-squares algorithm to minimize the chi-squared value:

$$\chi^2 = \sum_{i=1}^{N} \left(\frac{R_i}{\sigma_i} \right)^2, \tag{3}$$

where R_i is the residual of the ith TOA, σ_i is the uncertainty on the ith TOA, and the sum is performed over all of the TOAs used in the timing model (G. B. Hobbs et al. 2006). It is standard practice to rescale the TOA uncertainties so that the reduced χ^2 value of the timing solution is equal to 1. We note that this method may underestimate the true uncertainties of the final solutions in the presence of unmodeled trends in the residuals, however, we do not detect evidence of unmodeled red noise in any of our timing solutions, and take the given error bars as a reasonable estimate.

Under this formulation, a clear disparity arises between the two methods. Using folding, many single pulses which may arrive within a larger pulse envelope are averaged together into one pulse profile. On the other hand, each detected pulse may peak anywhere within a window that encompasses a few percent of the total rotational period of the source. These variations are intrinsic to the pulsar emission process; however, when these single-pulse TOAs are used to calculate a timing model, the large number of pulses with large residuals will yield a calculation of χ^2 and the rms residual value, which are much higher than the corresponding values in the integrated timing solution.

Hybrid timing models, formed from a combination of integrated and single-pulse TOAs, may be used for pulsars with infrequent observational cadences or small amounts of TOAs that make timing difficult. Epochs with single-pulse TOAs but no measurable integrated profile are common in the RRAT-like emission regime, but we also have observations with integrated TOAs but no single-pulse TOAs. These are typically short observations, with a small number of detected single pulses with S/N $\leqslant 7$, which are too dim to return a useful TOA measurement. While a hybrid method would be useful for extending timing baselines where necessary, the different uncertainty calculations for different types of TOAs would require more careful analysis for the derived timing parameters and their errors.

5.2. Pulse Jitter

On short timescales, the uncertainty in TOA measurements is dominated by radiometer noise, jitter noise, and scintillation noise (M. T. Lam et al. 2019). Radiometer noise typically dominates low S/N observations, as the limited sensitivity impacts the effectiveness of template matching. The single pulses from all pulsars vary stochastically in both shape and arrival phase, contributing an excess noise component known as pulse jitter. As observational sensitivity increases, pulse

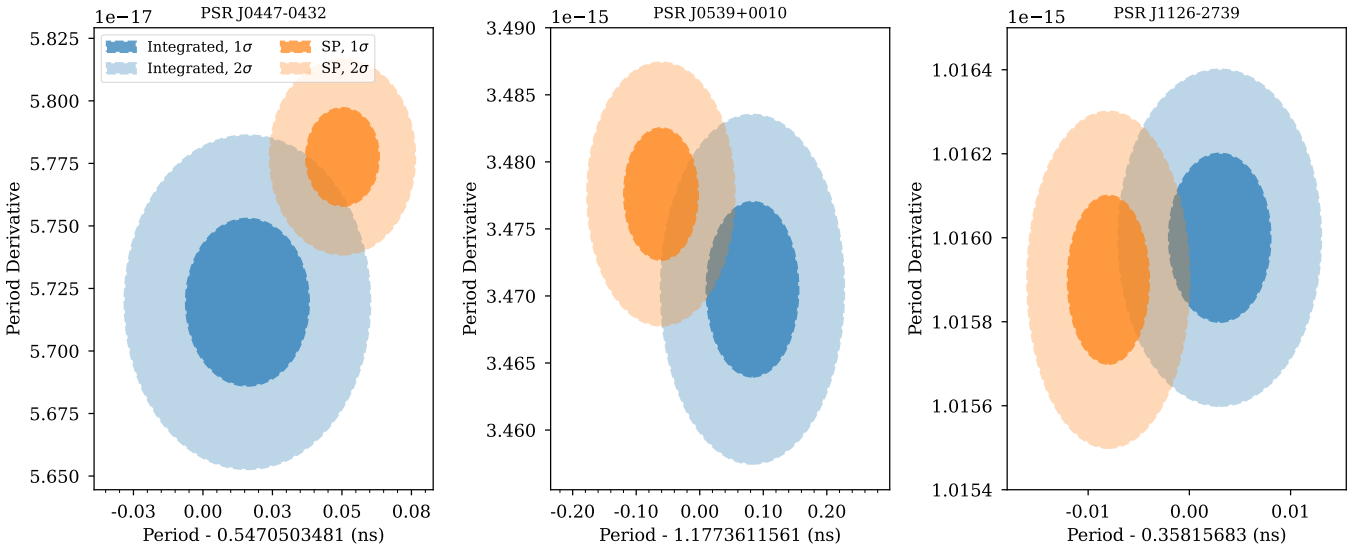

Figure 13. The period and period derivative found through pulsar timing for each pulsar, through integrated TOAs (blue) and single-pulse TOAs (orange). The 1σ and 2σ error bars on each parameter are denoted by the darker and lighter ellipses, respectively.

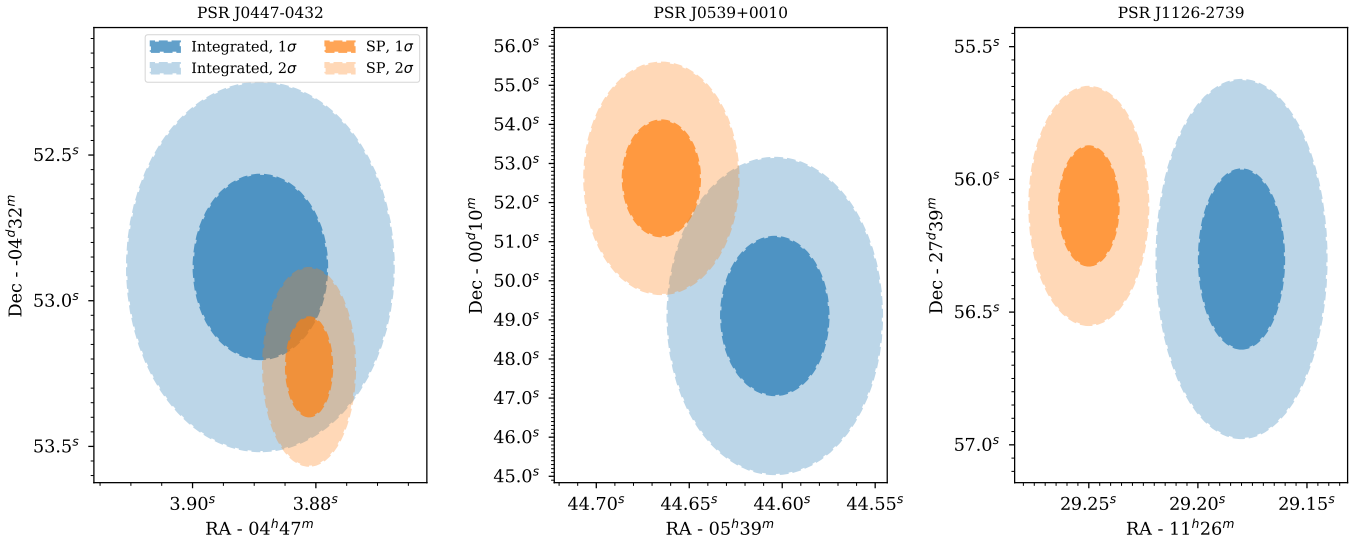

Figure 14. The R.A. and decl. coordinates found through pulsar timing for each pulsar, through integrated TOAs (blue) and single-pulse TOAs (orange). The 1σ and 2σ error bars on each parameter are denoted by the darker and lighter ellipses, respectively.

jitter is expected to become the dominant source of noise, especially for millisecond pulsars (M. T. Lam et al. 2019; X. L. Miao et al. 2023; S. Q. Wang et al. 2024). Previous estimates of the jitter-induced uncertainty have come either from cross-correlation of the TOA errors from different frequency bands (X. L. Miao et al. 2023) or by comparing the observed variance of the TOAs with the variance of idealized simulated datasets for each pulsar (A. Parthasarathy et al. 2021; S. Q. Wang et al. 2024), both of which are outside the scope of this work.

For each observational epoch, we calculate the mean TOA error of the integrated TOAs and compare this to the rms of all the single-pulse TOAs from that epoch. We only examined observations with more than five single-pulse TOAs and calculated the ratio of the single-pulse rms over the mean integrated TOA error. We find that the ratio varies between 5 and 25 for almost all of our observational epochs; averaging over all of the observations yields mean ratios of 19, 13, and 8 for PSRs J0447, J0539, and J1126 respectively.

5.3. Single-pulse Properties

In this work, we fitted log-normal and power-law functions to the normalized pulse energy distribution and found that power-law distributions are preferred for two of the pulsars. Despite this, we see no evidence of giant pulses with energies >10 times the average pulse energy, and all three pulsars show evidence of weak emission outside of the bright pulses. We conclude that the emission mechanisms at play here are fundamentally the same as for standard pulsars.

We also analyzed the wait time distributions of all three pulsars and found that Weibull distributions were preferred, implying moderate amounts of pulse clustering in time. While some pulses arrive consecutively, we do not exclusively observe "active" periods of several consecutive pulses followed by periods with no emission, and we are able to detect weak emission outside the bright pulses for each pulsar, leading us to conclude that these pulsars are not just extremely nulling pulsars.

6. Conclusion

We report phase-connected timing solutions for three radio pulsars discovered at 350 MHz with the GBNCC and GBT 350 MHz drift-scan surveys. Two of these pulsars were initially published as RRATs due to their discovery through single-pulse detection pipelines, but in subsequent observations, were sufficiently bright to form integrated pulse profiles and measure times of arrival. We formed two distinct timing models from different sets of TOAs: the integrated pulse profiles and the arrival times of all detected single pulses. The best-fit sky coordinates, period, and period derivative are in agreement within ∼2.5 standard deviations. The error bars on the parameters are of similar size between the two timing models, although the reported rms error of the single-pulse solutions are much higher for two of the pulsars owing to the large number of single pulses falling within a relatively wide phase envelope.

The wait-time distributions of each pulsar are better fit to a model in which pulses tend to be clustered together in time, suggesting that the pulses do not occur randomly or independently. The energy distributions tend to prefer power-law distributions, although no pulses meet the S/N > 10 threshold as a loose definition of "giant pulses," and the presence of weak emission outside the bright pulses indicates that these are weaker pulsars with sparse bright pulses, as is the case for many RRATs as they are observed with the next generation of more sensitive radio telescopes. This work shows the applicability of multiple TOA generation methods, and highlights the variety of emission characteristics of pulsars under the RRAT umbrella.

Acknowledgments

E.F.L. and M.A.M. are supported by NSF award AST-2009425. M.A.M. is also supported by NSF Physics Frontiers Center award PHYS-2020265. The Green Bank Observatory is a facility of the National Science Foundation operated under cooperative agreement by Associated Universities, Inc. The West Virginia University Research Corporation supported some of the GBT observations uses for this study.

Facility GBT (GUPPI).

Software: `Astropy` (https://www.astropy.org/; Astropy Collaboration et al. 2022), `Matplotlib` (https://matplotlib.org/; J. D. Hunter 2007), `Numpy` (https://numpy.org/; C. R. Harris et al. 2020), `PRESTO` (https://www.cv.nrao.edu/~sransom/presto/; S. Ransom 2011), `pyGDSM` (https://github.com/telegraphic/pygdsm; D. C. Price 2016), `Scipy` (https://scipy.org/; P. Virtanen et al. 2020), `seaborn` (https://github.com/mwaskom/seaborn; M. Waskom 2021), `TEMPO2` (https://www.atnf.csiro.au/research/pulsar/tempo2/; G. B. Hobbs et al. 2006).

ORCID iDs

E. F. Lewis https://orcid.org/0000-0002-2972-522X
M. A. McLaughlin https://orcid.org/0000-0001-7697-7422
J. K. Swiggum https://orcid.org/0000-0002-1075-3837
H. Blumer https://orcid.org/0000-0003-4046-884X
P. Chawla https://orcid.org/0000-0002-3426-7606
T. Dolch https://orcid.org/0000-0001-8885-6388
J. W. T. Hessels https://orcid.org/0000-0003-2317-1446
D. L. Kaplan https://orcid.org/0000-0001-6295-2881
V. Kaspi https://orcid.org/0000-0001-9345-0307
V. Kondratiev https://orcid.org/0000-0001-8864-7471
L. Levin https://orcid.org/0000-0002-2034-2986
R. S. Lynch https://orcid.org/0000-0001-5229-7430
J. G. Martinez https://orcid.org/0000-0003-0669-865X
A. E. McEwen https://orcid.org/0000-0001-5481-7559
E. Parent https://orcid.org/0000-0002-0430-6504
S. M. Ransom https://orcid.org/0000-0001-5799-9714
M. S. E. Roberts https://orcid.org/0000-0002-9396-9720
R. Spiewak https://orcid.org/0000-0002-6730-3298
I. H. Stairs https://orcid.org/0000-0001-9784-8670
K. Stovall https://orcid.org/0000-0002-7261-594X
J. van Leeuwen https://orcid.org/0000-0001-8503-6958

References

Abhishek, Malusare, N., Tanushree, N., Hegde, G., & Konar, S. 2022, JApA, 43, 75
Aloisi, R. J., Cruz, A., Daniels, L., et al. 2019, ApJ, 875, 19
Astropy Collaboration, Price-Whelan, A. M., Lim, P. L., et al. 2022, ApJ, 935, 167
Bezuidenhout, M. C., Barr, E., Caleb, M., et al. 2022, MNRAS, 512, 1483
Boyles, J., Lynch, R. S., Ransom, S. M., et al. 2013, ApJ, 763, 80
Burke-Spolaor, S., & Bailes, M. 2010, MNRAS, 402, 855
Burke-Spolaor, S., Johnston, S., Bailes, M., et al. 2012, MNRAS, 423, 1351
Cameron, A. D., Barr, E. D., Champion, D. J., Kramer, M., & Zhu, W. W. 2017, MNRAS, 468, 1994
Cordes, J. M., & McLaughlin, M. A. 2003, ApJ, 596, 1142
Cui, B.-Y., Boyles, J., McLaughlin, M. A., & Palliyaguru, N. 2017, ApJ, 840, 5
Doskoch, G. M., Basuroski, A., Halley, K., et al. 2024, ApJ, 973, 87
DuPlain, R., Ransom, S., Demorest, P., et al. 2008, SPIE, 7019, 70191D
Gao, S.-J., Li, X.-D., Yan, Z., Shao, Y.-X., & Zhou, P. 2025, ApJ, 991, 201
Gehrels, N. 1986, ApJ, 303, 336
Harris, C. R., Millman, K. J., van der Walt, S. J., et al. 2020, Natur, 585, 357
Hobbs, G. B., Edwards, R. T., & Manchester, R. N. 2006, MNRAS, 369, 655
Hunter, J. D. 2007, CSE, 9, 90
Jankowski, F., van Straten, W., Keane, E. F., et al. 2018, MNRAS, 473, 4436
Karako-Argaman, C., Kaspi, V. M., Lynch, R. S., et al. 2015, ApJ, 809, 67
Karuppusamy, R., Stappers, B. W., & van Straten, W. 2010, A&A, 515, A36
Kawash, A. M., McLaughlin, M. A., Kaplan, D. L., et al. 2018, ApJ, 857, 131
Keane, E. F., & Kramer, M. 2008, MNRAS, 391, 2009
Keane, E. F., & McLaughlin, M. A. 2011, BASI, 39, 333
Lam, M. T., McLaughlin, M. A., Arzoumanian, Z., et al. 2019, ApJ, 872, 193
Li, D., Wang, P., Qian, L., et al. 2018, IMMag, 19, 112
Lorimer, D. R., & Kramer, M. 2012, Handbook of Pulsar Astronomy (Cambridge University Press)
Lynch, R. S., Boyles, J., Ransom, S. M., et al. 2013, ApJ, 763, 81
Lynch, R. S., Swiggum, J. K., Kondratiev, V. I., et al. 2018, ApJ, 859, 93
Lyne, A. G., McLaughlin, M. A., Keane, E. F., et al. 2009, MNRAS, 400, 1439
Manchester, R. N., Hobbs, G. B., Teoh, A., & Hobbs, M. 2005, AJ, 129, 1993
McEwen, A. E., Spiewak, R., Swiggum, J. K., et al. 2020, ApJ, 892, 76
McLaughlin, M. A., Lyne, A. G., Keane, E. F., et al. 2009, MNRAS, 400, 1431
McLaughlin, M. A., Lyne, A. G., Lorimer, D. R., et al. 2006, Natur, 439, 817
Miao, X. L., Zhu, W. W., Kramer, M., et al. 2023, MNRAS, 526, 2156
Mickaliger, M. B., McEwen, A. E., McLaughlin, M. A., & Lorimer, D. R. 2018, MNRAS, 479, 5413
Mickaliger, M. B., McLaughlin, M. A., Lorimer, D. R., et al. 2012, ApJ, 760, 64
Oppermann, N., Yu, H.-R., & Pen, U.-L. 2018, MNRAS, 475, 5109
Parent, E., Kaspi, V. M., Ransom, S. M., et al. 2018, ApJ, 861, 44
Parthasarathy, A., Bailes, M., Shannon, R. M., et al. 2021, MNRAS, 502, 407
Price, D. C. 2016, PyGDSM: Python interface to Global Diffuse Sky Models, Astrophysics Source Code Library, ascl:1603.013

Ransom, S. 2011, PRESTO: PulsaR Exploration and Search TOolkit, Astrophysics Source Code Library, ascl:1107.017
Shapiro-Albert, B. J., McLaughlin, M. A., & Keane, E. F. 2018, ApJ, 866, 152
Stovall, K., Lynch, R. S., Ransom, S. M., et al. 2014, ApJ, 791, 67
Sun, S.-N., Yan, W.-M., Wang, N., & Yuen, R. 2021, RAA, 21, 240
van Leeuwen, A. G. J., Kouwenhoven, M. L. A., Ramachandran, R., Rankin, J. M., & Stappers, B. W. 2002, A&A, 387, 169
van Leeuwen, J., Mikhailov, K., Keane, E., et al. 2020, A&A, 634, A3
van Straten, W., Demorest, P., Khoo, J., et al. 2011, PSRCHIVE: Development Library for the Analysis of Pulsar Astronomical Data, Astrophysics Source Code Library, ascl:1105.014
Virtanen, P., Gommers, R., Oliphant, T. E., et al. 2020, NatMe, 17, 261
Wang, N., Manchester, R. N., & Johnston, S. 2007, MNRAS, 377, 1383
Wang, S. Q., Wang, N., Wang, J. B., et al. 2024, ApJ, 964, 6
Waskom, M. 2021, JOSS, 6, 3021
Zhou, D. J., Han, J. L., Xu, J., et al. 2023, RAA, 23, 104001